

Constraints on Ultra Heavy Dark Matter Properties from Dwarf Spheroidal Galaxies with LHAASO Observations

Zhen Cao,^{1,2,3} F. Aharonian,^{4,5} Q. An,^{6,7} Axikegu,⁸ Y.X. Bai,^{1,3} Y.W. Bao,⁹ D. Bastieri,¹⁰ X.J. Bi,^{1,2,3} Y.J. Bi,^{1,3} J.T. Cai,¹⁰ Q. Cao,¹¹ W.Y. Cao,⁷ Zhe Cao,^{6,7} J. Chang,¹² J.F. Chang,^{1,3,6} A.M. Chen,¹³ E.S. Chen,^{1,2,3} Liang Chen,¹⁴ Lin Chen,⁸ Long Chen,⁸ M.J. Chen,^{1,3} M.L. Chen,^{1,3,6} Q.H. Chen,⁸ S.H. Chen,^{1,2,3} S.Z. Chen,^{1,3} T.L. Chen,¹⁵ Y. Chen,⁹ N. Cheng,^{1,3} Y.D. Cheng,^{1,3} M.Y. Cui,¹² S.W. Cui,¹¹ X.H. Cui,¹⁶ Y.D. Cui,¹⁷ B.Z. Dai,¹⁸ H.L. Dai,^{1,3,6} Z.G. Dai,⁷ Danzengluobu,¹⁵ D. della Volpe,¹⁹ X.Q. Dong,^{1,2,3} K.K. Duan,¹² J.H. Fan,¹⁰ Y.Z. Fan,¹² J. Fang,¹⁸ K. Fang,^{1,3} C.F. Feng,²⁰ L. Feng,¹² S.H. Feng,^{1,3} X.T. Feng,²⁰ Y.L. Feng,¹⁵ S. Gabici,²¹ B. Gao,^{1,3} C.D. Gao,²⁰ L.Q. Gao,^{1,2,3} Q. Gao,¹⁵ W. Gao,^{1,3} W.K. Gao,^{1,2,3} M.M. Ge,¹⁸ L.S. Geng,^{1,3} G. Giacinti,¹³ G.H. Gong,²² Q.B. Gou,^{1,3} M.H. Gu,^{1,3,6} F.L. Guo,¹⁴ X.L. Guo,⁸ Y.Q. Guo,^{1,3} Y.Y. Guo,¹² Y.A. Han,²³ H.H. He,^{1,2,3} H.N. He,¹² J.Y. He,¹² X.B. He,¹⁷ Y. He,⁸ M. Heller,¹⁹ Y.K. Hor,¹⁷ B.W. Hou,^{1,2,3} C. Hou,^{1,3} X. Hou,²⁴ H.B. Hu,^{1,2,3} Q. Hu,^{7,12} S.C. Hu,^{1,2,3} D.H. Huang,⁸ T.Q. Huang,^{1,3} W.J. Huang,¹⁷ X.T. Huang,²⁰ X.Y. Huang,¹² Y. Huang,^{1,2,3} Z.C. Huang,⁸ X.L. Ji,^{1,3,6} H.Y. Jia,⁸ K. Jia,²⁰ K. Jiang,^{6,7} X.W. Jiang,^{1,3} Z.J. Jiang,¹⁸ M. Jin,⁸ M.M. Kang,²⁵ T. Ke,^{1,3} D. Kuleshov,²⁶ K. Kurinov,^{26,27} B.B. Li,¹¹ Cheng Li,^{6,7} Cong Li,^{1,3} D. Li,^{1,2,3} F. Li,^{1,3,6} H.B. Li,^{1,3} H.C. Li,^{1,3} H.Y. Li,^{7,12} J. Li,^{7,12} Jian Li,⁷ Jie Li,^{1,3,6} K. Li,^{1,3} W.L. Li,²⁰ W.L. Li,¹³ X.R. Li,^{1,3} Xin Li,^{6,7} Y.Z. Li,^{1,2,3} Zhe Li,^{1,3} Zhuo Li,²⁸ E.W. Liang,²⁹ Y.F. Liang,²⁹ S.J. Lin,¹⁷ B. Liu,⁷ C. Liu,^{1,3} D. Liu,²⁰ H. Liu,⁸ H.D. Liu,²³ J. Liu,^{1,3} J.L. Liu,^{1,3} J.Y. Liu,^{1,3} M.Y. Liu,¹⁵ R.Y. Liu,⁹ S.M. Liu,⁸ W. Liu,^{1,3} Y. Liu,¹⁰ Y.N. Liu,²² R. Lu,¹⁸ Q. Luo,¹⁷ H.K. Lv,^{1,3} B.Q. Ma,²⁸ L.L. Ma,^{1,3} X.H. Ma,^{1,3} J.R. Mao,²⁴ Z. Min,^{1,3} W. Mitthumsiri,³⁰ H.J. Mu,²³ Y.C. Nan,^{1,3} A. Neronov,²¹ Z.W. Ou,¹⁷ B.Y. Pang,⁸ P. Pattarakijwanich,³⁰ Z.Y. Pei,¹⁰ M.Y. Qi,^{1,3} Y.Q. Qi,¹¹ B.Q. Qiao,^{1,3} J.J. Qin,⁷ D. Ruffolo,³⁰ A. Sáiz,³⁰ D. Semikoz,²¹ C.Y. Shao,¹⁷ L. Shao,¹¹ O. Shchegolev,^{26,27} X.D. Sheng,^{1,3} F.W. Shu,³¹ H.C. Song,²⁸ Yu.V. Stenkin,^{26,27} V. Stepanov,²⁶ Y. Su,¹² Q.N. Sun,⁸ X.N. Sun,²⁹ Z.B. Sun,³² P.H.T. Tam,¹⁷ Q.W. Tang,³¹ Z.B. Tang,^{6,7} W.W. Tian,^{2,16} C. Wang,³² C.B. Wang,⁸ G.W. Wang,⁷ H.G. Wang,¹⁰ H.H. Wang,¹⁷ J.C. Wang,²⁴ K. Wang,⁹ L.P. Wang,²⁰ L.Y. Wang,^{1,3} P.H. Wang,⁸ R. Wang,²⁰ W. Wang,¹⁷ X.G. Wang,²⁹ X.Y. Wang,⁹ Y. Wang,⁸ Y.D. Wang,^{1,3} Y.J. Wang,^{1,3} Z.H. Wang,²⁵ Z.X. Wang,¹⁸ Zhen Wang,¹³ Zheng Wang,^{1,3,6} D.M. Wei,¹² J.J. Wei,¹² Y.J. Wei,^{1,2,3} T. Wen,¹⁸ C.Y. Wu,^{1,3} H.R. Wu,^{1,3} S. Wu,^{1,3} X.F. Wu,¹² Y.S. Wu,⁷ S.Q. Xi,^{1,3} J. Xia,^{7,12} J.J. Xia,⁸ G.M. Xiang,^{2,14} D.X. Xiao,¹¹ G. Xiao,^{1,3} G.G. Xin,^{1,3} Y.L. Xin,⁸ Y. Xing,¹⁴ Z. Xiong,^{1,2,3} D.L. Xu,¹³ R.F. Xu,^{1,2,3} R.X. Xu,²⁸ W.L. Xu,²⁵ L. Xue,²⁰ D.H. Yan,¹⁸ J.Z. Yan,¹² T. Yan,^{1,3} C.W. Yang,²⁵ F. Yang,¹¹ F.F. Yang,^{1,3,6} H.W. Yang,¹⁷ J.Y. Yang,¹⁷ L.L. Yang,¹⁷ M.J. Yang,^{1,3} R.Z. Yang,⁷ S.B. Yang,¹⁸ Y.H. Yao,²⁵ Z.G. Yao,^{1,3} Y.M. Ye,²² L.Q. Yin,^{1,3} N. Yin,²⁰ X.H. You,^{1,3} Z.Y. You,^{1,2,3} Y.H. Yu,⁷ Q. Yuan,¹² H. Yue,^{1,2,3} H.D. Zeng,¹² T.X. Zeng,^{1,3,6} W. Zeng,¹⁸ M. Zha,^{1,3} B.B. Zhang,⁹ F. Zhang,⁸ H.M. Zhang,⁹ H.Y. Zhang,^{1,3} J.L. Zhang,¹⁶ L.X. Zhang,¹⁰ Li Zhang,¹⁸ P.F. Zhang,¹⁸ P.P. Zhang,^{7,12} R. Zhang,^{7,12} S.B. Zhang,^{2,16} S.R. Zhang,¹¹ S.S. Zhang,^{1,3} X. Zhang,⁹ X.P. Zhang,^{1,3} Y.F. Zhang,⁸ Yi Zhang,^{1,12} Yong Zhang,^{1,3} B. Zhao,⁸ J. Zhao,^{1,3} L. Zhao,^{6,7} L.Z. Zhao,¹¹ S.P. Zhao,^{12,20} F. Zheng,³² B. Zhou,^{1,3} H. Zhou,¹³ J.N. Zhou,¹⁴ M. Zhou,³¹ P. Zhou,⁹ R. Zhou,²⁵ X.X. Zhou,⁸ C.G. Zhu,²⁰ F.R. Zhu,⁸ H. Zhu,¹⁶ K.J. Zhu,^{1,2,3,6} and X. Zuo^{1,3}

(The LHAASO Collaboration)*

¹Key Laboratory of Particle Astrophysics & Experimental Physics Division & Computing Center, Institute of High Energy Physics, Chinese Academy of Sciences, 100049 Beijing, China

²University of Chinese Academy of Sciences, 100049 Beijing, China

³Tianfu Cosmic Ray Research Center, 610000 Chengdu, Sichuan, China

⁴Dublin Institute for Advanced Studies, 31 Fitzwilliam Place, 2 Dublin, Ireland

⁵Max-Planck-Institut für Kernphysik, P.O. Box 103980, 69029 Heidelberg, Germany

⁶State Key Laboratory of Particle Detection and Electronics, China

⁷University of Science and Technology of China, 230026 Hefei, Anhui, China

⁸School of Physical Science and Technology & School of Information Science and Technology, Southwest Jiaotong University, 610031 Chengdu, Sichuan, China

⁹School of Astronomy and Space Science, Nanjing University, 210023 Nanjing, Jiangsu, China

¹⁰Center for Astrophysics, Guangzhou University, 510006 Guangzhou, Guangdong, China

¹¹Hebei Normal University, 050024 Shijiazhuang, Hebei, China

¹²Key Laboratory of Dark Matter and Space Astronomy & Key Laboratory of Radio Astronomy, Purple Mountain Observatory, Chinese Academy of Sciences, 210023 Nanjing, Jiangsu, China

¹³Tsung-Dao Lee Institute & School of Physics and Astronomy, Shanghai Jiao Tong University, 200240 Shanghai, China

¹⁴Key Laboratory for Research in Galaxies and Cosmology, Shanghai Astronomical Observatory, Chinese Academy of Sciences, 200030 Shanghai, China

- ¹⁵Key Laboratory of Cosmic Rays (Tibet University),
Ministry of Education, 850000 Lhasa, Tibet, China
- ¹⁶National Astronomical Observatories, Chinese Academy of Sciences, 100101 Beijing, China
- ¹⁷School of Physics and Astronomy (Zhuhai) & School of Physics (Guangzhou)
& Sino-French Institute of Nuclear Engineering and Technology (Zhuhai),
Sun Yat-sen University, 519000 Zhuhai & 510275 Guangzhou, Guangdong, China
- ¹⁸School of Physics and Astronomy, Yunnan University, 650091 Kunming, Yunnan, China
- ¹⁹Département de Physique Nucléaire et Corpusculaire, Faculté de Sciences,
Université de Genève, 24 Quai Ernest Ansermet, 1211 Geneva, Switzerland
- ²⁰Institute of Frontier and Interdisciplinary Science,
Shandong University, 266237 Qingdao, Shandong, China
- ²¹APC, Université Paris Cité, CNRS/IN2P3, CEA/IRFU, Observatoire de Paris, 119 75205 Paris, France
- ²²Department of Engineering Physics, Tsinghua University, 100084 Beijing, China
- ²³School of Physics and Microelectronics, Zhengzhou University, 450001 Zhengzhou, Henan, China
- ²⁴Yunnan Observatories, Chinese Academy of Sciences, 650216 Kunming, Yunnan, China
- ²⁵College of Physics, Sichuan University, 610065 Chengdu, Sichuan, China
- ²⁶Institute for Nuclear Research of Russian Academy of Sciences, 117312 Moscow, Russia
- ²⁷Moscow Institute of Physics and Technology, 141700 Moscow, Russia
- ²⁸School of Physics, Peking University, 100871 Beijing, China
- ²⁹School of Physical Science and Technology, Guangxi University, 530004 Nanning, Guangxi, China
- ³⁰Department of Physics, Faculty of Science, Mahidol University, 10400 Bangkok, Thailand
- ³¹Center for Relativistic Astrophysics and High Energy Physics,
School of Physics and Materials Science & Institute of Space Science and Technology,
Nanchang University, 330031 Nanchang, Jiangxi, China
- ³²National Space Science Center, Chinese Academy of Sciences, 100190 Beijing, China

(Dated: June 14, 2024)

In this work we try to search for signals generated by ultra-heavy dark matter at the Large High Altitude Air Shower Observatory (LHAASO) data. We look for possible gamma-ray by dark matter annihilation or decay from 16 dwarf spheroidal galaxies in the field of view of LHAASO. Dwarf spheroidal galaxies are among the most promising targets for indirect detection of dark matter which have low fluxes of astrophysical γ -ray background while large amount of dark matter. By analyzing more than 700 days observational data at LHAASO, no significant dark matter signal from 1 TeV to 1 EeV is detected. Accordingly we derive the most stringent constraints on the ultra-heavy dark matter annihilation cross-section up to EeV. The constraints on the lifetime of dark matter in decay mode are also derived.

Introduction— Various kinds of astronomical evidence suggest the existence of massive dark matter (DM) in the universe [1], which comprises approximately 85% of all matter [2]. However, DM cannot be explained by the Standard Model of particle physics [3, 4]. Therefore, one of the most important tasks in fundamental physics is to detect and reveal the nature of DM particles. Most searches primarily focus on weakly interacting massive particles (WIMPs) or ultra-light DM. However, no conclusive DM signal has been observed up to now [5–9]. On the other hand, ultra-heavy dark matter (UHDM; $10 \text{ TeV} \lesssim M_\chi \lesssim m_{pl} \approx 10^{16} \text{ TeV}$) represents a potential alternative DM candidate that could be generated through various mechanisms, including freeze-out, freeze-in, out-of-equilibrium decay, phase transitions, gravitational particle production, and primordial black holes (see the review in Ref. [10] and references therein). Some models for UHDM, like composite dark matter [11, 12], have been proposed to evade the unitarity limit, and very-high-energy (VHE) gamma-ray may be produced not only via the decay of UHDM, but also via its self-annihilation [13].

Among different astronomical systems, dwarf spheroidal galaxies (dSphs) are considered one of

the most promising targets for detecting DM signals due to their relatively short distances, high mass-to-light ratios [14, 15], and locations far away from complicated emission regions like the Galactic disk. These properties have instigated extensive research on them utilizing various astronomical facilities [16–23]. Importantly, given the relative proximity of these systems, the angular dimensions of their signal regions, particularly in scenarios involving decay, may be comparable to or even surpass the point spread function (PSF) of detection instruments. Thus, viewing these sources as extended rather than point-like sources may play a crucial role in the indirect detection of DM [24, 25].

The LHAASO is located in Sichuan Province, China, at an altitude of 4410 meters. It is a multi-purpose and comprehensive extensive air shower array, designed for the study of cosmic rays and gamma-ray across wide energy ranges, from 10 TeV to 100 PeV for cosmic rays and from sub-TeV to beyond 1 PeV for gamma-ray [26]. LHAASO is composed of three sub-arrays: the KiloMeter Squared Array (KM2A), the Water Cherenkov Detector Array (WCDA), and the Wide Field-of-view air Cherenkov Telescopes Array (WFCTA). Since its oper-

ation, several important results have been achieved in cosmic-ray and gamma-ray research [27–31]. The remarkable gamma-ray sensitivity of LHAASO for energies exceeding 100 TeV [32] presents an opportunity for the exploration of UHDM. WCDA and KM2A also have good PSFs for VHE gamma-ray [33, 34], enabling them to potentially discern the spatial extension of dSphs.

In this Letter, we search for VHE γ -ray signal from dSphs with data recorded by WCDA and KM2A of LHAASO, and report the stringent constraints on the UHDM up to EeV.

Gamma-ray Flux from Dark Matter—The expected differential gamma-ray flux from DM annihilation can be written as

$$\frac{dF_{\text{anni}}}{dE d\Omega dt}(E, \Omega) = \frac{\langle \sigma_{A\nu} \rangle}{8\pi M_\chi^2} \frac{dN_\gamma}{dE} e^{-\tau_{\gamma\gamma}(E)} \times \frac{dJ}{d\Omega}. \quad (1)$$

Similarly, for DM decay, it can be defined as

$$\frac{dF_{\text{decay}}}{dE d\Omega dt}(E, \Omega) = \frac{1}{4\pi\tau_\chi M_\chi} \frac{dN_\gamma}{dE} e^{-\tau_{\gamma\gamma}(E)} \times \frac{dD}{d\Omega}, \quad (2)$$

where $\langle \sigma_{A\nu} \rangle$ is the velocity-weighted DM annihilation cross-section, τ_χ is the DM decay lifetime, and M_χ is the mass of the DM particle. dN_γ/dE is the gamma-ray energy spectrum resulting from DM annihilation (decay), as calculated using HDMSpectra [35]. The term $\tau_{\gamma\gamma}(E)$ represents the total attenuation depth resulting from the pair production process ($\gamma\gamma \rightarrow e^+e^-$), taking into account background photons from starlight (SL), infrared radiation (IR), and cosmic microwave background (CMB), as described in Ref. [36]. The last term is the differential J- (D-) factor, which characterizes the strength of the DM signal. In Eq. 1 and Eq. 2, $dJ/d\Omega = \int \rho_{DM}^2(r) dl$, and $dD/d\Omega = \int \rho_{DM}(r) dl$, where $\rho_{DM}(r)$ refers to the DM density at distance r from the center of dSphs, and l represents the distance from a point on the line-of-sight (L.o.S) to the Earth. The J- (D-) factor is defined as the differential J- (D-) factor integrated over the region of interest (ROI). In this work, we take the DM density distribution in dSphs following the Navarro-Frenk-White (NFW) profile [37].

With a large field-of-view (FoV) of approximately 2 sr, LHAASO has the ability to observe about 60% of the sky each day [32]. The 16 dSphs within the FoV of LHAASO have been selected as our observation targets, and the coordinates of these dSphs are shown in Table S1 of the Supplemental Material [38]. To optimize the size of the ROI for balancing the preference between a larger area containing more signal and a smaller area with less background (and nearby sources) contamination, we utilize $\mathcal{S}/\sqrt{\mathcal{B}}$ as a metric, where \mathcal{S} and \mathcal{B} are the expected signal and expected background in the ROI, respectively. Considering the expected signal also

TABLE I. The ROI half width and J- (D-) factor for 16 dSphs considered in this analysis.

Name	$\log_{10}(J_\theta/\text{GeV}^2\text{cm}^{-5})$	$\theta_{\text{anni}}[\text{deg}]$	$\log_{10}(D_\theta/\text{GeVcm}^{-2})$	$\theta_{\text{decay}}[\text{deg}]$
Draco	$18.96^{+0.16}_{-0.15}$	1.0	$19.38^{+0.24}_{-0.32}$	2.3
Ursa Minor	$18.79^{+0.12}_{-0.11}$	1.0	$18.68^{+0.33}_{-0.15}$	2.1
Ursa Major I	$18.40^{+0.28}_{-0.27}$	0.9	$18.64^{+0.50}_{-0.48}$	1.8
Ursa Major II	$19.70^{+0.43}_{-0.43}$	1.0	$19.41^{+0.43}_{-0.57}$	2.0
Bootes I	$18.39^{+0.36}_{-0.37}$	0.9	$18.77^{+0.40}_{-0.54}$	1.8
Canes Venatici I	$17.43^{+0.16}_{-0.15}$	0.8	$18.19^{+0.40}_{-0.39}$	1.3
Coma Berenices	$19.26^{+0.35}_{-0.43}$	0.9	$19.12^{+0.46}_{-0.73}$	1.8
Leo I	$17.58^{+0.10}_{-0.10}$	0.8	$18.44^{+0.33}_{-0.42}$	1.4
Segue 1	$19.25^{+0.60}_{-0.69}$	0.8	$18.33^{+0.69}_{-0.63}$	0.8
Sextans	$17.80^{+0.10}_{-0.10}$	1.0	$18.49^{+0.28}_{-0.21}$	1.8
Canes Venatici II	$17.82^{+0.38}_{-0.37}$	0.8	$18.45^{+0.50}_{-0.74}$	1.4
Hercules	$17.60^{+0.53}_{-0.69}$	0.8	$17.70^{+0.62}_{-0.61}$	1.0
Leo II	$17.72^{+0.18}_{-0.17}$	0.8	$17.85^{+0.62}_{-0.40}$	1.0
Willman I	$19.80^{+0.50}_{-0.52}$	0.9	$19.00^{+0.71}_{-0.93}$	1.5
Aquarius 2	$18.57^{+0.50}_{-0.57}$	1.1	$18.53^{+0.61}_{-0.68}$	1.3
Leo T	$17.66^{+0.57}_{-0.52}$	0.8	$17.88^{+0.68}_{-0.69}$	1.0

depends on the details of NFW profile [39–41], we use the publicly available MCMC chains provided by Ref. [41] to determine the optimal ROI for our instrument and compute the corresponding J-(D-) factor distribution in our ROI. The details are discussed in Sec. II of the Supplemental Material. The half-width of the chosen ROI, the corresponding median J- (D-) factor, and its uncertainty for each dSph are shown in Table I. For the observation of WCDA, it is a conservative case that the ROI selection is consistent with the above value because WCDA has better angular resolution in the low energy range than KM2A. Meanwhile, the J- (D-) factor is consistent throughout the analysis.

Observation and Data Analysis—The present work utilizes LHAASO-WCDA data ($E < 20$ TeV) acquired from March 5, 2021 to March 31, 2023. LHAASO-KM2A data ($E > 10$ TeV) are utilized, including KM2A 1/2 array data from December 27, 2019 to November 30, 2020, KM2A 3/4 array data from December 1, 2020 to July 19, 2021, and KM2A full array data from July 20, 2021 to February 28, 2022. We apply the detector simulation, event reconstruction and selection algorithms detailed in the performance papers of LHAASO sub-arrays [33, 34] for the analysis of WCDA and KM2A data. The total effective observation time for each target dSph from WCDA and KM2A are shown in Table S1 of Supplemental Material [38].

We divide the KM2A data from 10 TeV to 10^3 TeV into 10 logarithmically evenly spaced bins according to reconstructed energy. For the WCDA data, events are divided into 6 groups according to the number of triggered PMT units (N_{hits}), i.e. [60,100], [100,200], [200,300], [300,500], [500,800], [800,2000]. Based on the reconstructed direction, the selected events from each energy bin in the KM2A dataset and each group of WCDA data are mapped onto a 2D sky map with a pixel size of $0.1^\circ \times 0.1^\circ$ in the equatorial coordinate. We use the “direct integration” method as described in Ref. [42] to estimate the number of background events per pixel. To elimi-

nate the contamination of known gamma-ray sources on background estimation, we mask the Galactic disk region ($|b| < 10^\circ$), known sources given by TeVCat [43], and first LHAASO catalog [44] (see Fig. S1 of Supplemental Material [38]).

The expected numbers of gamma-ray events produced by DM in the ROIs are calculated by folding the gamma-ray flux produced by DM with the WCDA and KM2A detector response function respectively. More details are discussed in Sec. I of Supplemental Material [38].

To quantify the excess of gamma-ray signals in the ROIs, we use a 3D binned likelihood ratio analysis combining WCDA and KM2A data. This method accounts for both the energy spectrum and the spatial characteristics of the DM signals, which are different from the background in the ROIs. In this analysis, we define the 3D likelihood function for the k -th dSph as follows:

$$\mathcal{L}_k = \prod_{i,j} \text{Poisson}(N_{i,j,k}^{obs}; N_{i,j,k}^{exp} + N_{i,j,k}^{bkg}) \times \mathcal{G}(B_k; B_k^{obs}, \sigma_k), \quad (3)$$

where

$$\mathcal{G}(B_k; B_k^{obs}, \sigma_k) = \frac{1}{\ln(10) B_k^{obs} \sqrt{2\pi} \sigma_k} \times e^{-[\log_{10}(B_k) - \log_{10}(B_k^{obs})]^2 / 2\sigma_k^2}. \quad (4)$$

The $N_{i,j,k}^{exp}$ is the expected number of gamma-ray from DM annihilation or decay in the i -th energy estimator bin and the j -th pixel on the 2D sky map of the k -th dSph. $N_{i,j,k}^{bkg}$ is the estimated background events from the ‘‘direct integration’’ method, and $N_{i,j,k}^{obs}$ is the observed number of gamma-ray photons. The term $\mathcal{G}(B_k; B_k^{obs}, \sigma_k)$ is included for the statistical uncertainties on the J- (D-) factor of the k -th dSph, following Ref. [16, 17], where B equals J for the annihilation case and B equals D for the decaying case. The larger uncertainties listed in Table I are taken as σ_k considering the asymmetric distribution of J- (D-) factor conservatively.

To quantify how well the DM signal fits the observed data, we define the test statistic of the k -th dSph (TS_k) as,

$$TS_k = -2\ln\left(\frac{\mathcal{L}_k(S=0)}{\mathcal{L}_k(S_{\max})}\right), \quad (5)$$

where S represents the DM signal flux, and S_{\max} is the best-fit value of the DM signal flux that maximizes the likelihood. To avoid non-physical values, we set $\langle\sigma_A v\rangle$ and τ_χ to be positive during the fitting process. We obtained the statistical significance of the signal over the null hypothesis (no DM model) by $\sqrt{TS_k}$. Then one-sided 95% confidence level (C.L.) limits on $\langle\sigma_A v\rangle$ or τ_χ are set by increasing the DM signal normalization

from its best-fit value until $-2\ln\mathcal{L}$ increases by a value of 2.71 [45].

The combined likelihood analysis of all dSphs is performed by $\mathcal{L}_{total} = \prod_k \mathcal{L}_k$, with the aim of improving the overall statistical power and generating stronger constraints on the DM parameters.

Results— We utilize data from 756 days of LHAASO-WCDA and 794 days of LHAASO-KM2A observations to search for DM signals in 16 dSphs around the Milky Way. No significant gamma-ray excess was detected from these dSphs. The statistical significance of DM signals in these dSphs is shown in Sec. III of Supplemental Material [38]. Therefore, 95% C.L. limits are placed on the DM annihilation cross-section or the DM decay lifetime, as shown in Fig. 1 and Fig. 2 respectively. In Fig. S8 of Supplemental Material [38], the 95% C.L. upper limits for $\langle\sigma_A v\rangle$ from combined and individual dSphs are presented, assuming a DM mass range from 1 TeV to 1 EeV with a 100% branching ratio to specific standard model particles. The combined upper limits are dominated by sources with large J-factor, small uncertainties and favorable locations inside the LHAASO FoV, i.e., Ursa Major II, Ursa Minor, Draco, Willman I, Segue 1 and Coma Berenices.

To assess the consistency between the constraints derived from the observed data and the expected limits from pure background, we repeat 1000 mock observations under the null hypothesis, considering the Poisson fluctuation with the measured background. The expected combined limits and the two-sided 68% and 95% containment bands for $b\bar{b}$ and $\tau^+\tau^-$ are shown in Fig. 1. See also Fig. S10 of the Supplemental Material [38] for other channels. The fact that observed limits are between the expected limit bands indicates that the observational data are consistent with Poisson fluctuation with the background. The constraints on high-mass DM consistently approach the 68% boundary of the anticipated limit bands, suggesting a slight overestimation of the background in this study and thereby a deficit in the number of putative signal events inferred in the ROIs. This overestimation is likely due to the contribution of faint sources which are below our sensitivity threshold and thus not removed by the mask used in our background estimation; this issue may be more important for high masses due to the lower event rates at high energies. Fig. 1 also shows the ‘‘Thermal Relic’’ cross-section [47] and the limits from other experiments such as Fermi-LAT [17], HAWC [19], H.E.S.S [20], MAGIC [21], VERITAS [22], and IceCube [46]. The observations of dSphs by LHAASO could provide better constraints for DM with a mass heavier than a few hundred TeV.

In Fig. S9 of Supplemental Material [38], the 95% C.L. lower limits for τ_χ are presented for combined and individual dSphs analysis. Similar to the DM annihilation results, the limits are mainly driven by Ursa Major II,

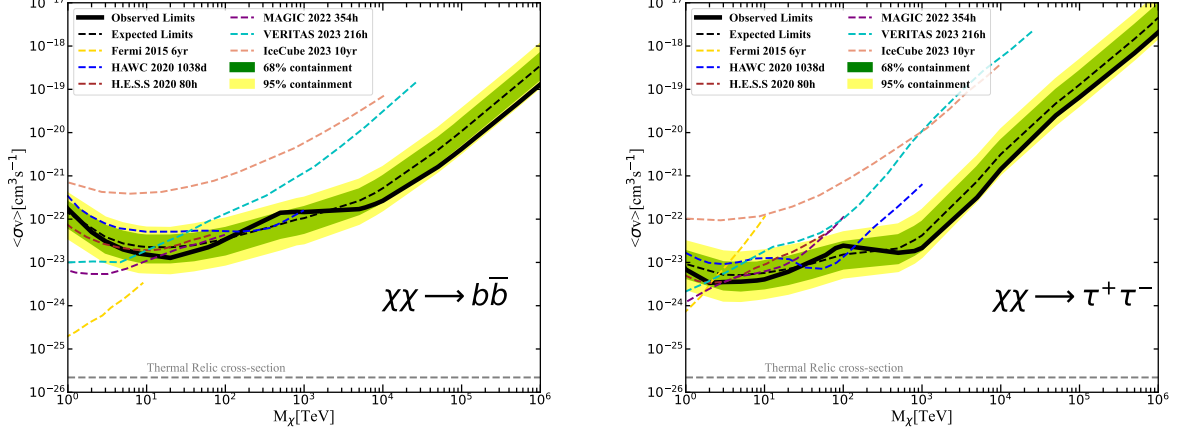


FIG. 1. The 95% C.L. upper limits on the DM annihilation cross-section for $b\bar{b}, \tau^+\tau^-$ channels and comparing to other experiments (Fermi-LAT [17], HAWC [19], H.E.S.S. [20], MAGIC [21], VERITAS [22], IceCube [46]). The solid black line represents the observed combined limit of this work. The dashed black line, green band, and yellow band represent the expected limits and their 1σ and 2σ uncertainties. The dashed gray line is Thermal Relic cross-section [47], and the other dashed colored lines show the results of other experiments.

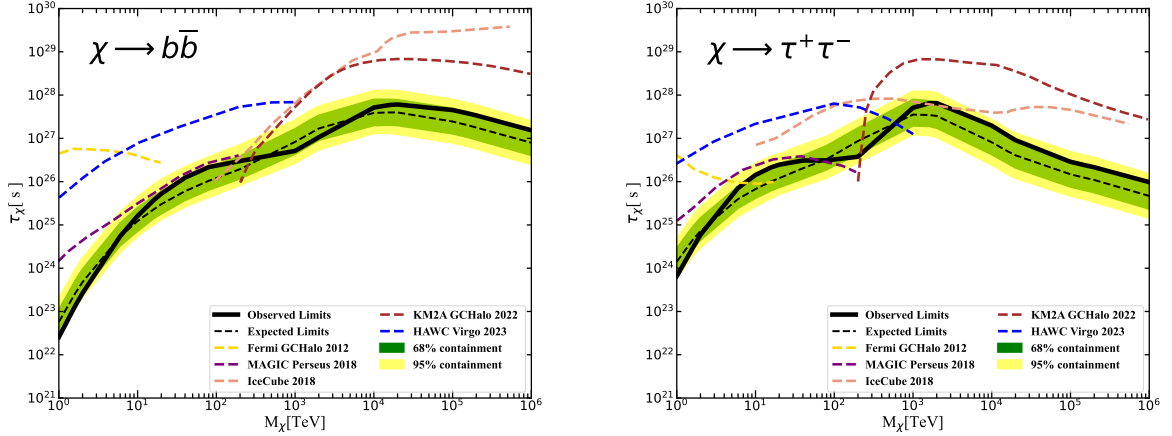


FIG. 2. The 95% C.L. lower limits on the DM decay lifetime for $b\bar{b}, \tau^+\tau^-$ channels. The solid black line represents the LHAASO observed combined limit, and the dashed black line, green band, and yellow band represent the expected combined limits, 1σ and 2σ uncertainty based on the mock observation. The limits obtained from Fermi-LAT [48], MAGIC [49], IceCube [50], LHAASO-KM2A Galactic halo [29] and HAWC [51] with dashed colored line are also shown for comparison.

Ursa Minor, Draco, and Coma Berenices. The expected limits from the same analysis for mock data are shown in Fig. 2, for $b\bar{b}$ and $\tau^+\tau^-$ final states, with the limits from Fermi-LAT [48], MAGIC [49], IceCube [50], LHAASO-KM2A Galactic halo [29], and HAWC [51]. We also show constraints for τ_χ from combined dSphs observation and mock data in Fig. S10 of Supplemental Material [38] for other channels.

In our analysis, we incorporate the J- (D-) factor likelihood into our likelihood analysis, leading to a reduc-

tion in the constraints on DM parameters by a factor of 2-6 (see Fig. S6 of Supplemental Material [38]). Additionally, we factor in the effects of VHE gamma-ray absorption by the ISRF, resulting in a relaxation of constraints on DM particles with masses exceeding 1000 TeV by approximately 5-10-fold. Moreover, we consider the expected morphology of the DM signal, moving beyond a point-like source approximation. The constraints derived from the extended source analysis based on the DM density profile are consequently diminished by a factor of

1.5-12, particularly in the context of DM decay scenarios, conforming a strong effect of the spatial extension of dSphs on the DM search results [25]. It is important to acknowledge that the J- (D-) factor correction exclusively accounts for the statistical uncertainties in the J- (D-) factors and does not address the systematic uncertainties stemming from the choice of DM profiles and uncertainties with some presumptions about Jeans equation. While factors such as departures from spherical symmetry, velocity anisotropy of the DM halo, the influence of contaminating foreground stars, and variations in the DM profile are considered, the predicted J- (D-) factors and constraints may undergo alterations by a few-fold [17, 52–58].

Our results extend for the first time the mass range of the limits on the $\langle\sigma_{AV}\rangle$ to 1 EeV with the best constraints above a few hundred TeV. Fermi-LAT [17], H.E.S.S [20], MAGIC [21], and VERITAS [22] exhibit more stringent limits at lower DM masses, since the effective area of LHAASO would decay rapidly at low energy. We have comparable limits to HAWC [19] for masses up to several hundred TeV and consistently have better constraints than those from IceCube [46] across all mass ranges. For the DM decay lifetime, our constraints are weaker than those based on galactic halo data by KM2A [29], since the D-factor in the selected dSphs is smaller, and the effects of attenuation by pair production are more significant considering the large distances of dSphs from the Earth compared to the galactic halo. In general, our constraints on the DM decay lifetime are also less stringent compared to those determined by HAWC [51], MAGIC [49], Fermi-LAT [48], and IceCube [50] through the observation of Virgo cluster, Perseus cluster, and the galactic halo with larger D-factors and subdominant effects of attenuation. However, the combined limits from dSphs, considering the uncertainties of the DM distribution and the spatial extension of the expected signal, could also provide a complementary set of reliable limits.

Conclusion and Outlook— We investigate DM annihilation and decay signals from 16 dSphs within the LHAASO FoV using data collected by WCDA and KM2A. No significant gamma-ray excess is observed from these sources. Consequently, we establish individual and combined constraints on $\langle\sigma_{AV}\rangle$ and τ_χ across five channels ($b\bar{b}, t\bar{t}, \mu^+\mu^-, \tau^+\tau^-, W^+W^-$).

In this analysis, we treat the selected dSphs as extended sources in the 3D likelihood analysis framework to consider the spatial distribution of the DM density within the dSphs. We optimize the size of ROIs and recalculate the J- (D-) factor and their uncertainties corresponding to the ROIs. To make the analysis more comprehensive and reliable, the absorption effect of ISRF on VHE gamma-ray is considered, and the statistical uncertainty of the J- (D-) factor is incorporated as a nuisance parameter in the likelihood analysis.

Our results represent the first-ever constraint on $\langle\sigma_{AV}\rangle$,

extending the mass of DM to 1 EeV. The combined limits are the most stringent constraints for $\langle\sigma_{AV}\rangle$ above a few hundred TeV. Meanwhile, we stress that the impact of spatial extension from dSphs is a necessary condition when deriving DM limits from dSphs with future instruments. As more WCDA and KM2A data will be collected, the development of algorithms to enhance energy and angular resolution for LHAASO, and improvements in kinematics measurements to reduce the uncertainty of the DM density distribution, LHAASO is expected to become more sensitive and to improve its limits in the future.

Acknowledgements— We would like to thank all staff members who work at the LHAASO site above 4400 meters above sea level year-round to maintain the detector and keep the water recycling system, electricity power supply and other components of the experiment operating smoothly. We are grateful to Chengdu Management Committee of Tianfu New Area for the constant financial support for research with LHAASO data. This research work is supported by the following grants: The National Key R&D program of China No.2018YFA0404201, No.2018YFA0404202, No.2018YFA0404203, No.2018YFA0404204, National Natural Science Foundation of China No.12175248, No.12322302, Department of Science and Technology of Sichuan Province, China No.2021YFSY0030, Project for Young Scientists in Basic Research of Chinese Academy of Sciences No.YSBR-061, the Chinese Academy of Sciences, the Program for Innovative Talents and Entrepreneur in Jiangsu, and in Thailand by the National Science and Technology Development Agency (NSTDA) and the National Research Council of Thailand (NRCT) under the High-Potential Research Team Grant Program (N42A650868).

* Corresponding Author:

jiakang@mail.sdu.edu.cn (K. Jia)

lij@pmo.ac.cn (J. Li)

bixj@ihep.ac.cn (X.J. Bi)

gaolinqing@hotmail.com (L.Q. Gao)

xyhuang@pmo.ac.cn (X.Y. Huang)

liwl@mail.sdu.edu.cn (W.L. Li)

zhucg@email.sdu.edu.cn (C.G. Zhu)

- [1] G. Bertone *et al.*, Particle dark matter: evidence, candidates and constraints, *Physics Reports* **405**, 279 (2005).
- [2] N. Aghanim *et al.* (Planck), Planck 2018 results. VI. Cosmological parameters, *Astron. Astrophys.* **641**, A6 (2020), [Erratum: *Astron. Astrophys.* 652, C4 (2021)], [arXiv:1807.06209 \[astro-ph.CO\]](https://arxiv.org/abs/1807.06209).
- [3] G. Jungman *et al.*, Supersymmetric dark matter, *Physics Reports* **267**, 195 (1996).
- [4] L. Bergström, Dark matter evidence, particle physics candidates and detection methods, *Annalen der Physik* **524**, 479 (2012).

- [5] F. Alemanno *et al.* (DAMPE), Search for gamma-ray spectral lines with the DArk Matter Particle Explorer, *Sci. Bull.* **67**, 679 (2022), arXiv:2112.08860 [astro-ph.HE].
- [6] H. An, S. Ge, W.-Q. Guo, X. Huang, J. Liu, and Z. Lu, Direct Detection of Dark Photon Dark Matter Using Radio Telescopes, *Phys. Rev. Lett.* **130**, 181001 (2023), arXiv:2207.05767 [hep-ph].
- [7] J. W. Foster, S. J. Witte, M. Lawson, T. Linden, V. Gajjar, C. Weniger, and B. R. Safdi, Extraterrestrial Axion Search with the Breakthrough Listen Galactic Center Survey, *Phys. Rev. Lett.* **129**, 251102 (2022), arXiv:2202.08274 [astro-ph.CO].
- [8] J. Aalbers *et al.* (LZ), First Dark Matter Search Results from the LUX-ZEPLIN (LZ) Experiment, *Phys. Rev. Lett.* **131**, 041002 (2023), arXiv:2207.03764 [hep-ex].
- [9] E. Aprile *et al.* (XENON), First Dark Matter Search with Nuclear Recoils from the XENONnT Experiment, *Phys. Rev. Lett.* **131**, 041003 (2023), arXiv:2303.14729 [hep-ex].
- [10] D. Carney *et al.*, Snowmass2021 cosmic frontier white paper: Ultraheavy particle dark matter, *SciPost Physics Core* **6**, 10.21468/scipostphyscore.6.4.075 (2023).
- [11] K. Harigaya *et al.*, Thermal relic dark matter beyond the unitarity limit, *Journal of High Energy Physics* **2016**, 10.1007/jhep08(2016)151 (2016).
- [12] M. Geller *et al.*, Dark quarkonium formation in the early universe, *Journal of High Energy Physics* **2018**, 135 (2018).
- [13] D. Tak *et al.*, Current and future gamma-ray searches for dark matter annihilation beyond the unitarity limit, *The Astrophysical Journal Letters* **938**, L4 (2022).
- [14] L. E. Strigari, Galactic searches for dark matter, *Physics Reports* **531**, 1 (2013).
- [15] J. Conrad *et al.*, Indirect dark matter searches in gamma and cosmic rays, *Nature Physics* **13**, 224 (2017).
- [16] M. Ackermann *et al.* (Fermi-LAT), Constraining Dark Matter Models from a Combined Analysis of Milky Way Satellites with the Fermi Large Area Telescope, *Phys. Rev. Lett.* **107**, 241302 (2011), arXiv:1108.3546 [astro-ph.HE].
- [17] M. Ackermann *et al.* (The Fermi-LAT Collaboration), Searching for dark matter annihilation from milky way dwarf spheroidal galaxies with six years of fermi large area telescope data, *Phys. Rev. Lett.* **115**, 231301 (2015).
- [18] A. Albert *et al.*, Dark matter limits from dwarf spheroidal galaxies with the HAWC gamma-ray observatory, *The Astrophysical Journal* **853**, 154 (2018).
- [19] A. Albert *et al.*, Search for gamma-ray spectral lines from dark matter annihilation in dwarf galaxies with the high-altitude water cherenkov observatory, *Phys. Rev. D* **101**, 103001 (2020).
- [20] H. Abdallah *et al.* (H.E.S.S. Collaboration), Search for dark matter signals towards a selection of recently detected des dwarf galaxy satellites of the milky way with h.e.s.s., *Phys. Rev. D* **102**, 062001 (2020).
- [21] V. Acciari *et al.*, Combined searches for dark matter in dwarf spheroidal galaxies observed with the magic telescopes, including new data from coma berenices and draco, *Physics of the Dark Universe* **35**, 100912 (2022).
- [22] A. Acharyya *et al.*, Search for ultraheavy dark matter from observations of dwarf spheroidal galaxies with veritas, *The Astrophysical Journal* **945**, 101 (2023).
- [23] W.-Q. Guo, Y. Li, X. Huang, Y.-Z. Ma, G. Beck, Y. Chandola, and F. Huang, Constraints on dark matter annihilation from the FAST observation of the Coma Berenices dwarf galaxy, *Phys. Rev. D* **107**, 103011 (2023), arXiv:2209.15590 [astro-ph.HE].
- [24] M. Ackermann *et al.* (Fermi-LAT), Search for Dark Matter Satellites using the FERMI-LAT, *Astrophys. J.* **747**, 121 (2012), arXiv:1201.2691 [astro-ph.HE].
- [25] M. Di Mauro, M. Stref, and F. Calore, Investigating the effect of Milky Way dwarf spheroidal galaxies extension on dark matter searches with Fermi-LAT data, *Phys. Rev. D* **106**, 123032 (2022), arXiv:2212.06850 [astro-ph.HE].
- [26] X.-H. Ma *et al.*, Chapter 1 lhaaso instruments and detector technology *, *Chinese Physics C* **46**, 030001 (2022).
- [27] Z. Cao *et al.*, Ultrahigh-energy photons up to 1.4 petaelectronvolts from 12 gamma-ray galactic sources, *Nature* **594**, 33 (2021).
- [28] Z. Cao *et al.* (LHAASO Collaboration), Exploring lorentz invariance violation from ultrahigh-energy γ rays observed by lhaaso, *Phys. Rev. Lett.* **128**, 051102 (2022).
- [29] Z. Cao *et al.* (LHAASO Collaboration), Constraints on heavy decaying dark matter from 570 days of lhaaso observations, *Phys. Rev. Lett.* **129**, 261103 (2022).
- [30] V. Aharonian *et al.* (LHAASO Collaboration), Extended very-high-energy gamma-ray emission surrounding psr J0622 + 3749 observed by lhaaso-km2a, *Phys. Rev. Lett.* **126**, 241103 (2021).
- [31] Z. Cao *et al.*, A tera-electron volt afterglow from a narrow jet in an extremely bright gamma-ray burst, *Science* **380**, 1390 (2023).
- [32] C. Zhen *et al.*, Introduction to large high altitude air shower observatory (lhaaso), *Chinese Astronomy and Astrophysics* **43**, 457 (2019).
- [33] F. Aharonian *et al.*, Performance of lhaaso-wcda and observation of the crab nebula as a standard candle *, *Chinese Physics C* **45**, 085002 (2021).
- [34] F. Aharonian *et al.*, Observation of the crab nebula with lhaaso-km2a -a performance study, *Chinese Physics C* **45**, 025002 (2021).
- [35] C. W. Bauer *et al.*, Dark matter spectra from the electroweak to the planck scale, *Journal of High Energy Physics* **2021**, 10.1007/jhep06(2021)121 (2021).
- [36] A. Esmaili *et al.*, Gamma-ray bounds from EAS detectors and heavy decaying dark matter constraints, *Journal of Cosmology and Astroparticle Physics* **2015** (10), 014.
- [37] J. F. Navarro *et al.*, A universal density profile from hierarchical clustering, *The Astrophysical Journal* **490**, 493 (1997).
- [38] See Supplemental Material at [URL will be inserted by publisher] for additional details and results, which includes Refs. [59–62].
- [39] A. Geringer-Sameth *et al.*, Dwarf galaxy annihilation and decay emission profiles for dark matter experiments, *The Astrophysical Journal* **801**, 74 (2015).
- [40] V. Bonnard *et al.*, Dark matter annihilation and decay in dwarf spheroidal galaxies: the classical and ultrafaint dsphs, *Monthly Notices of the Royal Astronomical Society* **453**, 849–867 (2015).
- [41] A. B. Pace *et al.*, Scaling relations for dark matter annihilation and decay profiles in dwarf spheroidal galaxies, *Monthly Notices of the Royal Astronomical Society* **482**, 3480–3496 (2018).
- [42] R. Fleysher *et al.*, Tests of statistical significance and background estimation in gamma-ray air shower experi-

- ments, *The Astrophysical Journal* **603**, 355 (2004).
- [43] S. P. Wakely and D. Horan, TeVCat: An online catalog for Very High Energy Gamma-Ray Astronomy, in *30th International Cosmic Ray Conference*, Vol. 3 (2007) pp. 1341–1344.
- [44] Z. Cao *et al.* (LHAASO), The First LHAASO Catalog of Gamma-Ray Sources, *Astrophys. J. Suppl.* **271**, 25 (2024), [arXiv:2305.17030 \[astro-ph.HE\]](#).
- [45] G. Cowan *et al.*, Asymptotic formulae for likelihood-based tests of new physics, *The European Physical Journal C* **71**, 10.1140/epjc/s10052-011-1554-0 (2011).
- [46] X.-K. Guo *et al.*, Searching for dark-matter induced neutrino signals in dwarf spheroidal galaxies using 10 years of icecube public data, *Phys. Rev. D* **108**, 043001 (2023).
- [47] G. Steigman *et al.*, Precise relic wimp abundance and its impact on searches for dark matter annihilation, *Phys. Rev. D* **86**, 023506 (2012).
- [48] M. Ackermann *et al.*, Constraints on the galactic halo dark matter from fermi-lat diffuse measurements, *The Astrophysical Journal* **761**, 91 (2012).
- [49] V. Acciari *et al.*, Constraining dark matter lifetime with a deep gamma-ray survey of the perseus galaxy cluster with magic, *Physics of the Dark Universe* **22**, 38 (2018).
- [50] M. G. Aartsen *et al.*, Search for neutrinos from decaying dark matter with icecube, *The European Physical Journal C* **78**, 831 (2018).
- [51] A. Albert *et al.* (HAWC Collaboration), Search for decaying dark matter in the virgo cluster of galaxies with hawc, *Phys. Rev. D* **109**, 043034 (2024).
- [52] V. Bonnivard, C. Combet, D. Maurin, and M. G. Walker, Spherical Jeans analysis for dark matter indirect detection in dwarf spheroidal galaxies - Impact of physical parameters and triaxiality, *Mon. Not. Roy. Astron. Soc.* **446**, 3002 (2015), [arXiv:1407.7822 \[astro-ph.HE\]](#).
- [53] V. Bonnivard, D. Maurin, and M. G. Walker, Contamination of stellar-kinematic samples and uncertainty about dark matter annihilation profiles in ultrafaint dwarf galaxies: the example of Segue I, *Mon. Not. Roy. Astron. Soc.* **462**, 223 (2016), [arXiv:1506.08209 \[astro-ph.GA\]](#).
- [54] N. Klop, F. Zandanel, K. Hayashi, and S. Ando, Impact of axisymmetric mass models for dwarf spheroidal galaxies on indirect dark matter searches, *Phys. Rev. D* **95**, 123012 (2017), [arXiv:1609.03509 \[astro-ph.CO\]](#).
- [55] J. L. Sanders, N. W. Evans, A. Geringer-Sameth, and W. Dehnen, Indirect Dark Matter Detection for Flattened Dwarf Galaxies, *Phys. Rev. D* **94**, 063521 (2016), [arXiv:1604.05493 \[astro-ph.GA\]](#).
- [56] K. Ichikawa, M. N. Ishigaki, S. Matsumoto, M. Ibe, H. Sugai, K. Hayashi, and S.-i. Horigome, Foreground effect on the J -factor estimation of classical dwarf spheroidal galaxies, *Mon. Not. Roy. Astron. Soc.* **468**, 2884 (2017), [arXiv:1608.01749 \[astro-ph.GA\]](#).
- [57] P. Ullio and M. Valli, A critical reassessment of particle Dark Matter limits from dwarf satellites, *JCAP* **07**, 025, [arXiv:1603.07721 \[astro-ph.GA\]](#).
- [58] K. Hayashi, K. Ichikawa, S. Matsumoto, M. Ibe, M. N. Ishigaki, and H. Sugai, Dark matter annihilation and decay from non-spherical dark halos in galactic dwarf satellites, *Mon. Not. Roy. Astron. Soc.* **461**, 2914 (2016), [arXiv:1603.08046 \[astro-ph.GA\]](#).
- [59] Z. Cao *et al.* (LHAASO), Measurement of Ultra-High-Energy Diffuse Gamma-Ray Emission of the Galactic Plane from 10 TeV to 1 PeV with LHAASO-KM2A, *Phys. Rev. Lett.* **131**, 151001 (2023), [arXiv:2305.05372 \[astro-ph.HE\]](#).
- [60] X. Huang and K. Duan, A 3D Likelihood Analysis Tool for LHAASO-KM2A data, *PoS ICRC2021*, 769 (2021).
- [61] T. P. Li and Y. Q. Ma, Analysis methods for results in gamma-ray astronomy, *Astrophys. J.* **272**, 317 (1983).
- [62] D. E. Alexandreas *et al.*, Point source search techniques in ultrahigh-energy gamma-ray astronomy, *Nucl. Instrum. Meth. A* **328**, 570 (1993).

SUPPLEMENTAL MATERIAL

I. DATA ANALYSIS WITH LHAASO

Table S1 shows the equatorial coordinates and the effective observation time of LHAASO for target dSphs in this analysis, where the T_{WCDA} and T_{KM2A} represent the effective observation time of LHAASO-WCDA and LHAASO-KM2A respectively.

Fig S1 displays the masked sky map during background estimation in the equatorial coordinate system. In this work, we mask the Galactic disk region ($|b| < 10^\circ$), known sources given by TeVCat [43] and first LHAASO catalog [44] with exclusion radius $R_{\text{excl}} = n \cdot \sqrt{\sigma_{\text{ext}}^2 + \sigma_{\text{psf}}^2}$, where $n = 2.5$ is a constant factor, σ_{ext} and σ_{psf} denote the sources extension and the PSF of instruments respectively, as in Ref. [59].

Detector response for gamma-ray is crucial to relate the DM flux to the number of events from the dSphs. We investigate the detector response of LHAASO-WCDA and LHAASO-KM2A to detect gamma-ray as a function of the primary energy and the incidence direction from same detector simulation procedure in performance paper[33, 34]. Following Ref. [60], the expected events ($N_{i,j,k}^{\text{DM}}$) of gamma-ray from DM annihilation or decay in i -th energy estimator bin and j -th pixel of 2D sky map for k -th dSph in the observation time is calculated by

$$N_{i,j,k}^{\text{DM}} = \int_i d\eta \int_j d\Omega(\hat{p}') \int dt R(\eta, \hat{p}', t), \quad (6)$$

where the η is the energy estimator, which represented as the number of triggered PMTs (N_{hit}) for WCDA, and represented as reconstruction energy for KM2A. The \hat{p}' represents the reconstructed direction according to the direction reconstruction algorithm and t denotes the observation time. As for the R , it can be described by the following formation,

$$R(\eta, \hat{p}', t) = \int dE \int_{\hat{p}} d\Omega \frac{dF}{dE d\Omega dt} A(\hat{p}, E) P(\hat{p}', E; \hat{p}) M(\eta, \hat{p}; E). \quad (7)$$

Here, the E and \hat{p} are the primary energy and primary direction for a gamma-ray event. The flux term is expected differential gamma-ray flux from DM annihilation or decay, which is described as Eq.1 and Eq.2 of the Letter. These three factors are computed for once LHAASO observation, effective collection area ($A(\hat{p}, E)$), point-spread-function ($P(\hat{p}', E; \hat{p})$) and energy estimator transfer matrix ($M(\eta, \hat{p}; E)$). According to LHAASO official simulation data[33, 34], the effective area is the product of reference area and efficiency from event trigger, reconstruction and selection for gamma-ray with primary energy E and primary direction \hat{p} . The point spread function and the energy estimator transfer matrix are the probability distributions of the reconstructed direction \hat{p}' and the observed energy estimator with primary

energy E and primary direction \hat{p} respectively. With the expected events of gamma-ray from DM, $N_{i,j,k}^{\text{DM}}$, and estimated background events, we could get the expected numbers of gamma-ray, $N_{i,j,k}^{\text{exp}}$, in the i -th energy estimator (N_{hit} for WCDA and reconstructed energy for KM2A) bin and the j -th pixel on the 2D sky map of the k -th dSph.

II. CALCULATION FOR J- (D-) FACTOR AND DENSITY PROFILE

The observation targets referred in this work are selected from Ref. [41]. Among the 44 dSphs objects studied in Ref. [41], we exclude the 6 dSphs bound to Andromeda Galaxy (M31) and 15 dSphs that are not in LHAASO's FoV, where the declination of dSphs satisfies the range -20.64° to 79.36° . Subsequently, from the remaining 23 dSphs, we select 16 dSphs as our primary observation targets. The coordinates of these selected dSphs are detailed in Table S1. Notably, apart from their advantageous locations, these chosen dSphs exhibit tighter constraints compared to the unselected dSphs. The seven dSphs within LHAASO's FoV which the authors of Ref. [41] indicate should be treated with caution because the MCMC chains include tails or provide only upper limits in posterior distributions (Draco II, Leo IV, Leo V, Pisces II, Pegasus III, Segue 2 and Triangulum II), are not selected for the study.

In Eq. 1 and Eq. 2 of the Letter, $dJ/d\Omega$ and $dD/d\Omega$ are defined as,

$$\frac{dJ}{d\Omega} = \int \rho_{\text{DM}}^2(r) dl, \quad (8)$$

$$\frac{dD}{d\Omega} = \int \rho_{\text{DM}}(r) dl, \quad (9)$$

where the $\rho_{\text{DM}}(r)$ refers to the DM density profile in the dSphs, and l represents the distance from a point on the line-of-sight (L.o.S) to the Earth. The relationship between r and l is described by $r^2 = l^2 + d^2 - 2ld\cos\theta$. Here, d represents the distance between the dSph center and the Earth, while θ denotes the angle between the L.o.S and the direction of the dSph center. In this work, Navarro–Frenk–White (NFW)[37] model is adopted as

$$\rho_{\text{DM}}(r) = \frac{\rho_s}{(r/r_s)(1+r/r_s)^2}, \quad (10)$$

where ρ_s is the scale density and r_s is the scale radius. The upper limits of integration of l are conservatively estimated with the tidal radius (r_t) of dSphs [41], as

$$l_{\pm} = d\cos(\theta) \pm \sqrt{r_t^2 - d^2\sin^2(\theta)}. \quad (11)$$

TABLE S1. The associated the right ascension, the declination, and the effective observation time (day) of WCDA and KM2A for 16 dSphs within the LHAASO FoV.

Name	Ra[deg]	Dec[deg]	T _{WCDA} [day]	T _{KM2A} [day]
Draco	260.05	57.92	690.37	730.76
Ursa Minor	227.28	67.23	701.59	739.53
Ursa Major I	158.71	51.92	692.51	742.17
Ursa Major II	132.87	63.13	688.88	740.83
Bootes 1	210.02	14.50	699.85	742.01
Canes Venatici I	202.02	33.56	699.01	743.28
Coma Berenices	186.74	23.90	696.88	744.34
Leo I	152.12	12.30	692.19	743.02
Segue 1	151.77	16.08	691.72	743.06
Sextans	153.26	-1.61	693.36	743.60
Canes Venatici II	194.29	34.32	698.15	743.81
Hercules	247.76	12.79	699.04	737.33
Leo II	168.37	22.15	693.95	744.18
Willman I	162.34	51.05	693.45	742.21
Aquarius 2	338.48	-9.33	666.84	728.11
Leo T	143.72	17.05	690.84	742.51

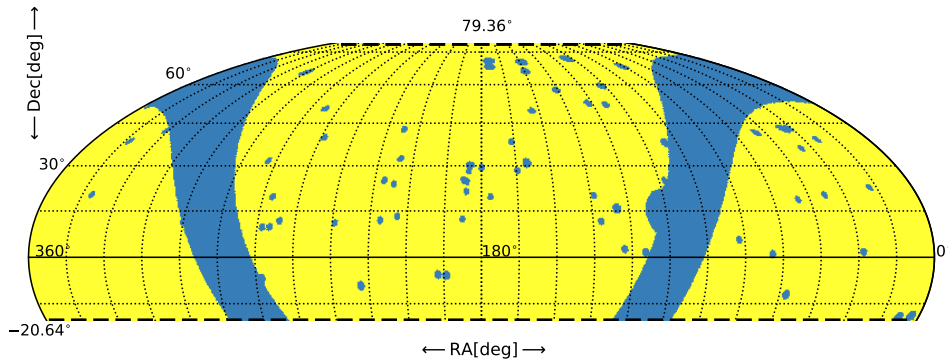


FIG. S1. The masked sky map in the equatorial coordinate system.

The parameters (i.e. d , r_t , ρ_s , r_s) determine the calculation of the density profile and the J- (D-) factor of dSphs. The Ref [41] performed a Jeans analysis on the target dSphs, whose DM profiles follow the NFW profile with these parameters mentioned above. We use their public available MCMC chains to calculate the distribution of density profile and J- (D-) for each target dSph. Fig S2 shows the constraints on the differential J- (D-) profile for two dSphs: the classical dwarf Draco and the ultra-faint dwarf Ursa Major II. The envelopes show the $\pm 1\sigma$ and median values of the differential J- (D-) profile as a function of the angular separation from the center of the dSphs.

In order to maximize the sensitivity of the signal

search, we use $\mathcal{S}/\sqrt{\mathcal{B}}$ as an indicator to find the optimal region of interest (ROI) [61], where \mathcal{S} is the 2D signal map, which use the J- (D-) profile of each dSphs convolved with 2D point spread function (PSF) at first KM2A energy estimator bin and multiply by the solid angle in each pixel. \mathcal{B} is background distribution estimated according to the background estimation method mentioned in data analysis. We sum all signal within θ to get \mathcal{S} and sum all background within θ to get \mathcal{B} , and we vary θ to maximize $\mathcal{S}/\sqrt{\mathcal{B}}$. We obtain the variation of the signal-to-noise ratio ($\mathcal{S}/\sqrt{\mathcal{B}}$) with the angle θ , and select the θ with the maximum median signal-to-noise ratio as the ROI size. Fig S3 shows the DM annihilation signal-to-noise ratio as a function of the θ for the

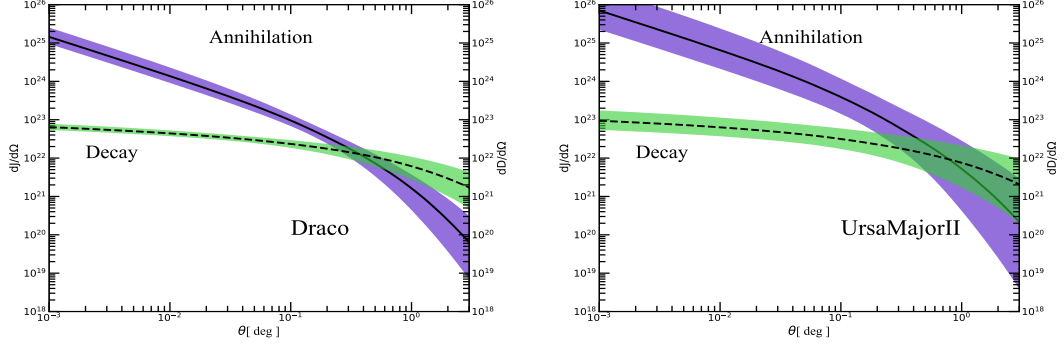


FIG. S2. Expected differential J- profile (purple) and D- profile (green) for Draco and Ursa Major II. At each angle the solid and dashed lines show the median profiles and the shaded band corresponds to the $\pm 1\sigma$ distribution as derived in MCMC chains provided by Ref [41].

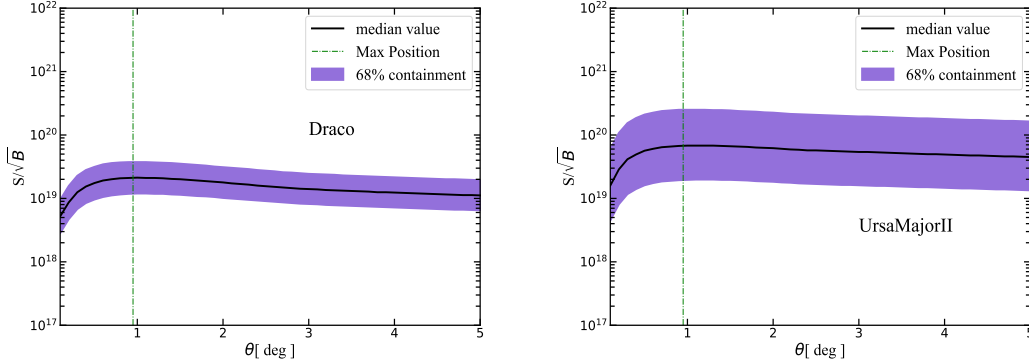


FIG. S3. The DM annihilation signal-to-noise ratio as a function of the angle for the Draco (left) and Ursa Major II (right). The black solid line represents the median curve of signal-to-noise ratio, and the shaded band corresponds to the $\pm 1\sigma$ distribution. The maximum value of the median curve is represented by the green dashed line, corresponding to the optimal region.

TABLE S2. The corresponding density profile parameters of J- factor for each dSphs [41].

Source	d/kpc	r_t/kpc	$\log_{10}(\rho_s/M_\odot \text{kpc}^{-3})$	$\log_{10}(r_s/\text{kpc})$
Draco	67.40	9.07	7.45	0.17
Ursa Minor	73.29	6.92	7.91	-0.18
Ursa Major I	95.58	8.34	7.83	-0.19
Ursa Major II	35.12	9.35	6.79	0.72
Bootes 1	65.69	9.06	6.62	0.58
Canes Venatici I	211.09	19.82	7.20	0.14
Coma Berenices	42.31	5.14	7.57	0.06
Leo I	266.15	23.25	7.72	-0.09
Segue 1	23.88	3.41	6.96	0.39
Sextans	89.63	11.88	6.32	0.65
Canes Venatici II	166.26	29.91	6.50	0.70
Hercules	138.16	22.21	6.17	0.82
Leo II	242.44	19.15	7.95	-0.23
Willman I	44.46	8.07	7.81	0.10
Aquarius 2	107.50	24.46	6.59	0.78
Leo T	380.69	25.00	6.69	0.74

Draco and Ursa Major II, in which the black solid line represents the median curve of signal-to-noise ratio, and the maximum value of the median is represented by the green dashed line, corresponding to the optimal region. The optimal regions for some dSphs are smaller than the

PSF of KM2A at first KM2A energy estimator bin, in which case we fixed the selected ROI as 1.58σ [62], and use the parameters corresponding to the median of the J-(D-) factor at the optimal ROI as the parameters of the dark matter distribution model, as shown in Table S2. The ROI sizes and J- (D-) factors of the 16 dSphs are shown in Table I in the Letter.

III. STATISTICAL SIGNIFICANCE OF DM ANNIHILATION AND DECAY SIGNALS

The significance map of two dSphs, the classical dwarf Draco and the ultra-faint dwarf Ursa Major II, are calculated by using the Li-Ma formula [61] with KM2A and WCDA data, as shown in Fig S4. The dashed green and red lines in the figures indicate the ROI regions for DM decay and annihilation, respectively.

Fig S5 shows the signal significance as a function of dark matter particle mass in the two channels, i.e., $b\bar{b}$ and

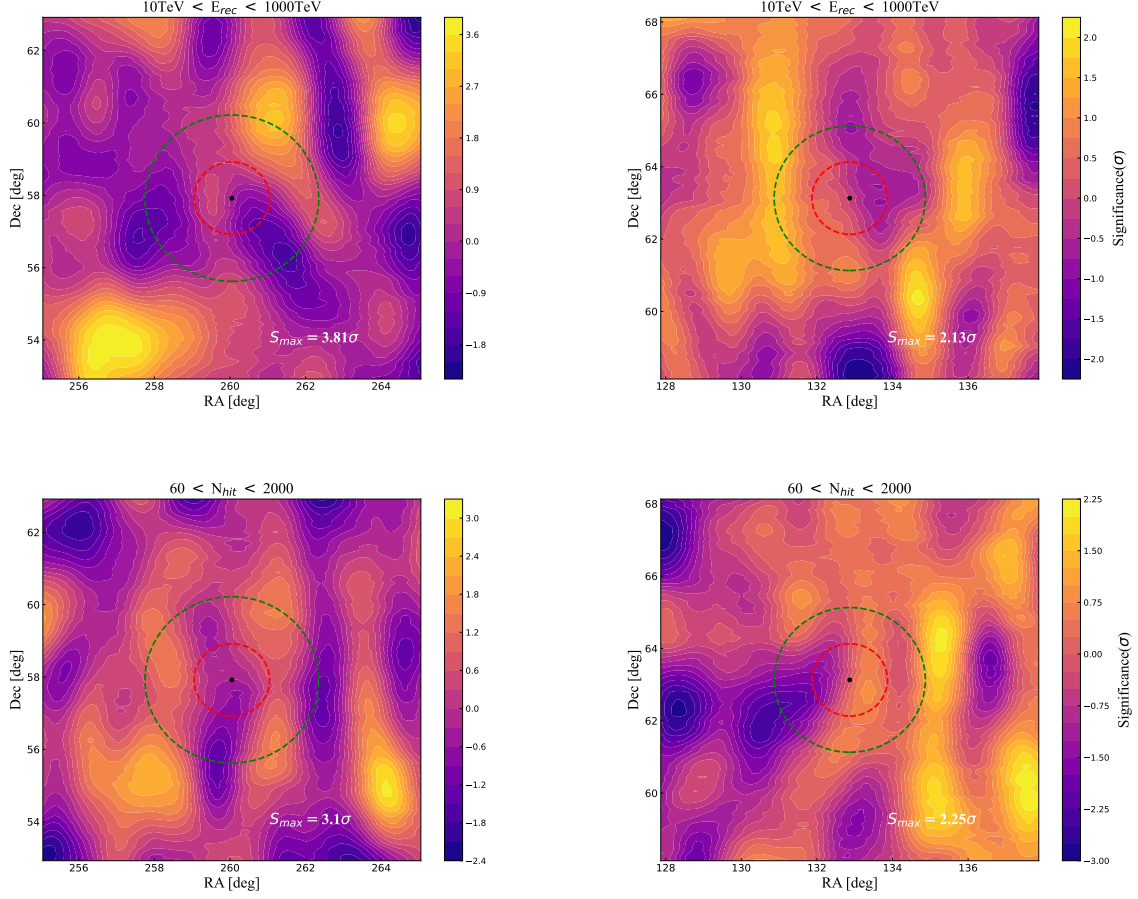


FIG. S4. The significance map of Draco (left) and Ursa Major II (right) of the energy of 10-1000 TeV in the KM2A data (top) and N_{hit} of 60-2000 in the WCDA data (bottom).

$\tau^+\tau^-$. There is no significant gamma-ray signal excess from the dark matter annihilation or decay process in this analysis, with the highest significance approaching 2.4σ .

IV. OTHER SUPPLEMENTARY RESULTS

In Fig S6, we show comparison of results for the impacts of High Energy gamma-ray absorption by the Interstellar Radiation Field (ISRF), uncertainty of J- (D-) factor and morphology processing of dSphs on DM parameter constraints.

In Fig S7, we show comparison of results for the impacts of treating dSphs as point sources versus extended sources, using WCDA data only, KM2A data only, and combined WCDA and KM2A data. It is clear that, in the case of KM2A data, constraints on low-mass dark mat-

ter remain consistent between point source and extended source analyses, which is consistent with the large PSF at lower energy levels. However, constraints on high-mass dark matter are degraded significantly in the extended analysis due to the high-quality PSF at higher energy levels. Similar trends in constraints are observed in the results obtained from WCDA. As anticipated, the signal originating from decay processes should exhibit even greater spatial extension compared to that from annihilation. Thus it is evident that the good PSF of LHAASO could enable us to take the spatial analysis.

In Fig S8 and Fig S9, we show 95% C.L. upper limits on the DM annihilation cross-section and 95% C.L. lower limits on the DM decay lifetime from individual analysis of each dSph and combined analysis of all dSphs.

In Fig S10, we show the comparison of observed limits and expected limits from pure background simulation.

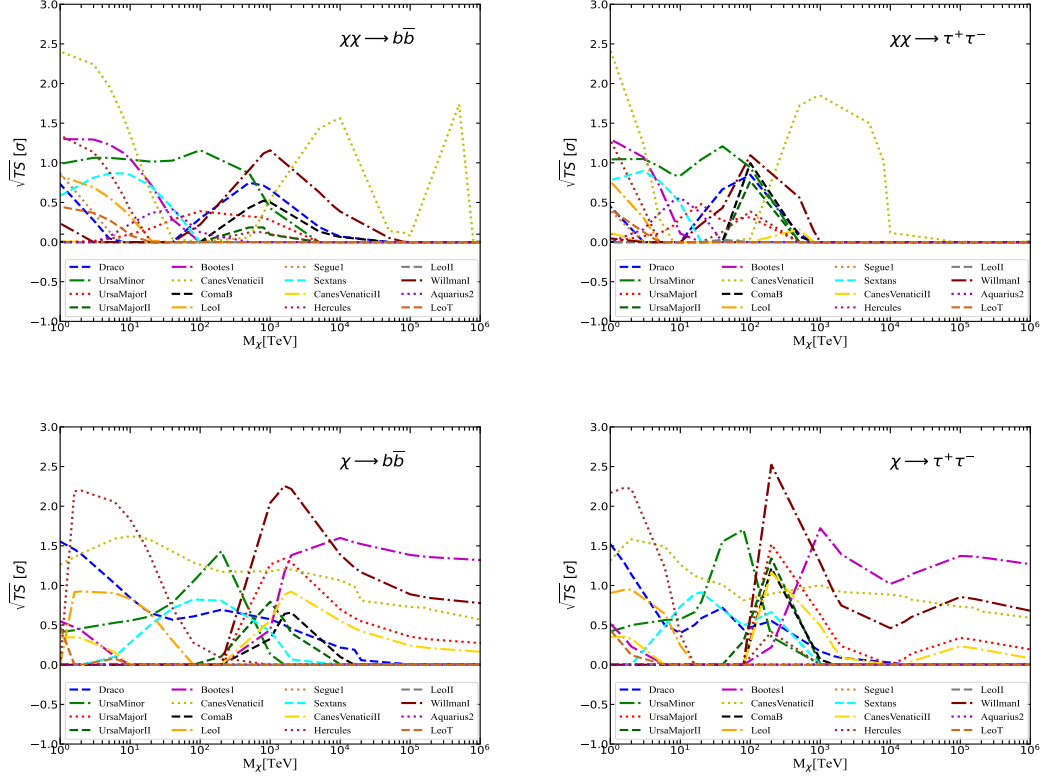


FIG. S5. LHAASO-measured significance of the dark matter annihilation (top panel) and decay (bottom panel) signal in two channels, i.e., $b\bar{b}$ and $\tau^+\tau^-$, for the 16 individual dSphs. The color lines show the signal significance for each dSphs as a function of dark matter particle mass.

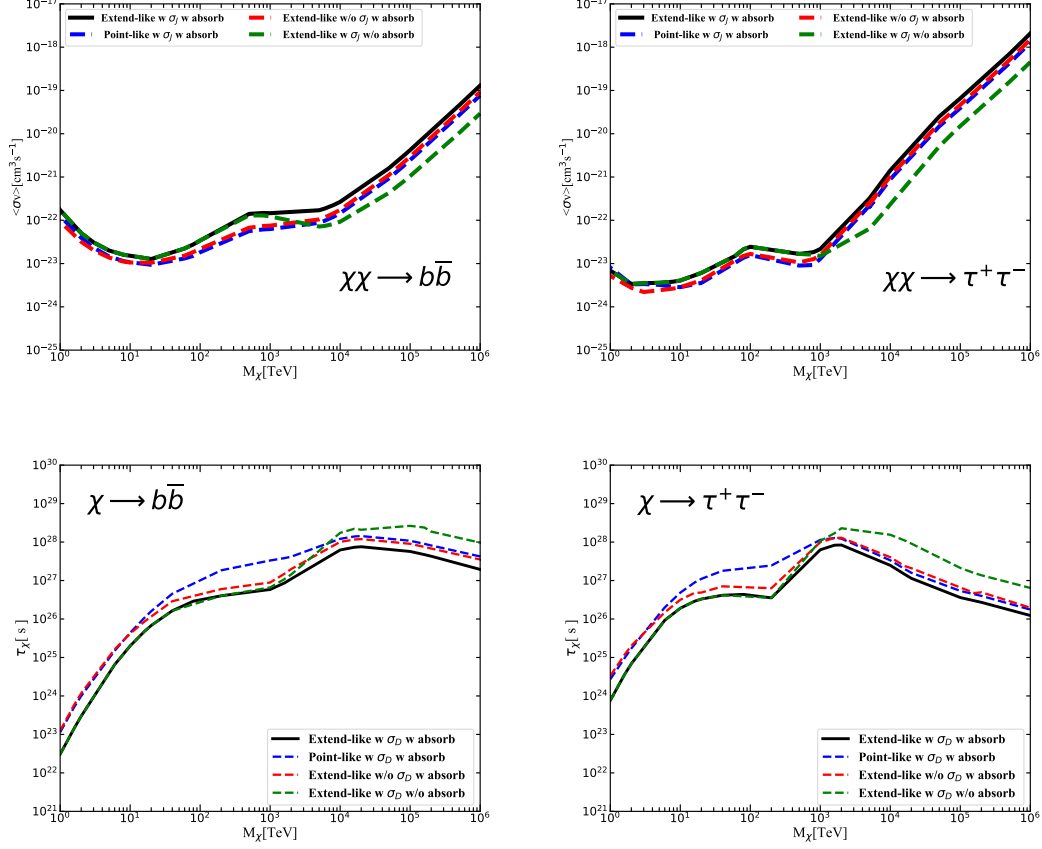


FIG. S6. Comparison of results for the impacts of high energy gamma-ray absorption by the Interstellar Radiation Field (ISRF), uncertainty of J- (D-) factor and morphology processing of dSphs on DM parameter constraints. The top panels represent the compared combined limits of DM annihilation cross-section of $b\bar{b}$ and $\tau^+\tau^-$ channels, while down panels represent the compared combined limits of DM decay lifetime. The black line represents the limits of the extended source analysis with J- (D-) factor uncertainty and the effect of absorption, as the benchmark analysis. The dashed green line represents the limits of the extended source analysis considering only the J- (D-) factor uncertainty, and the dashed red line represents the results of the extended source analysis considering only the effect of absorption by ISRF. The dashed blue line represents the limits of the point-like source analysis with J- (D-) factor uncertainty and the effect of absorption by ISRF.

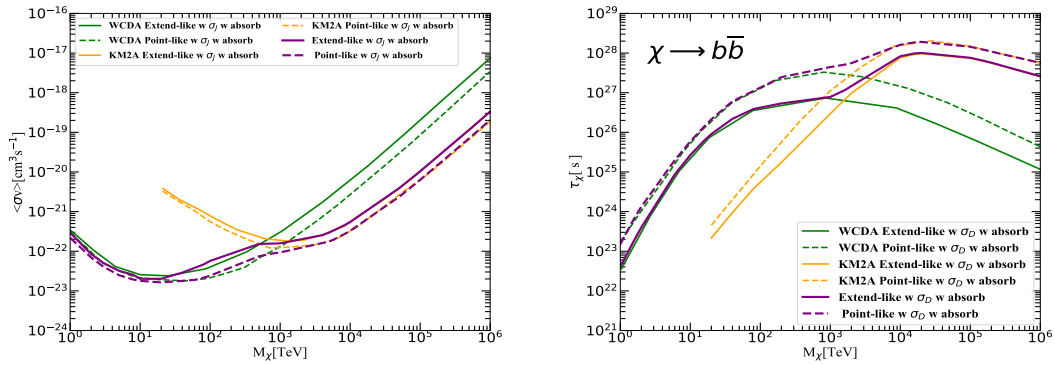


FIG. S7. Comparison of results for the impacts of treating dSphs as point sources versus extended sources, using WCDA data only, KM2A data only, and combined WCDA and KM2A data. The 95% C.L. upper limits on the DM annihilation cross-section for the $b\bar{b}$ channels are shown in the left panel. The 95% C.L. lower limits on the DM lifetime for the $b\bar{b}$ channels are presented in the right panel.

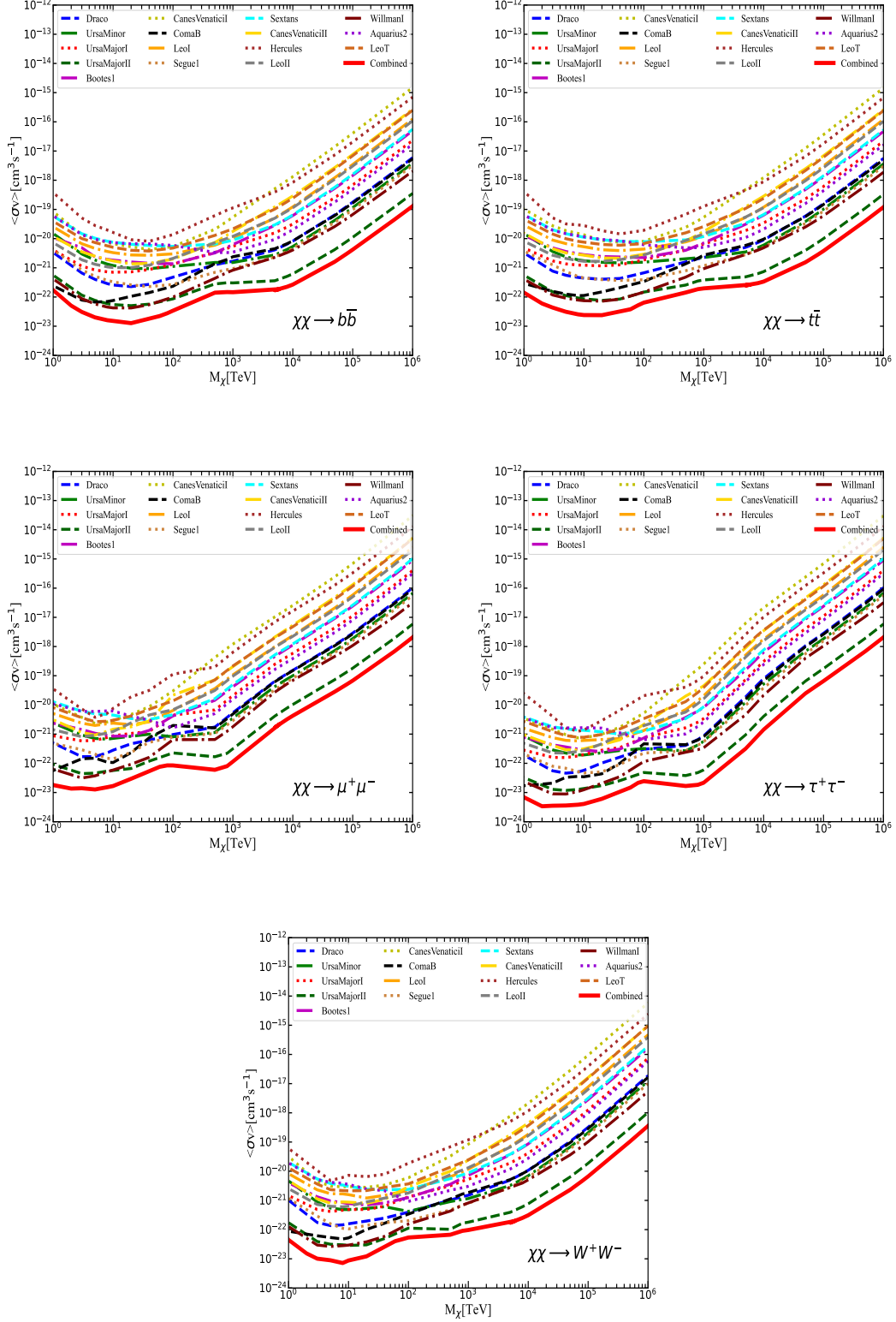


FIG. S8. The results of LHAASO analysis show the 95% C.L. upper limits on the DM annihilation cross-section for five channels ($b\bar{b}, \tau^+\tau^-, t\bar{t}, \mu^+\mu^-$ and W^+W^-) using data from 16 dSphs around the Milky Way. The solid red line represents the combined limits obtained using all of the dSphs, while the dashed colored lines represent the individual upper limits obtained from each dSph.

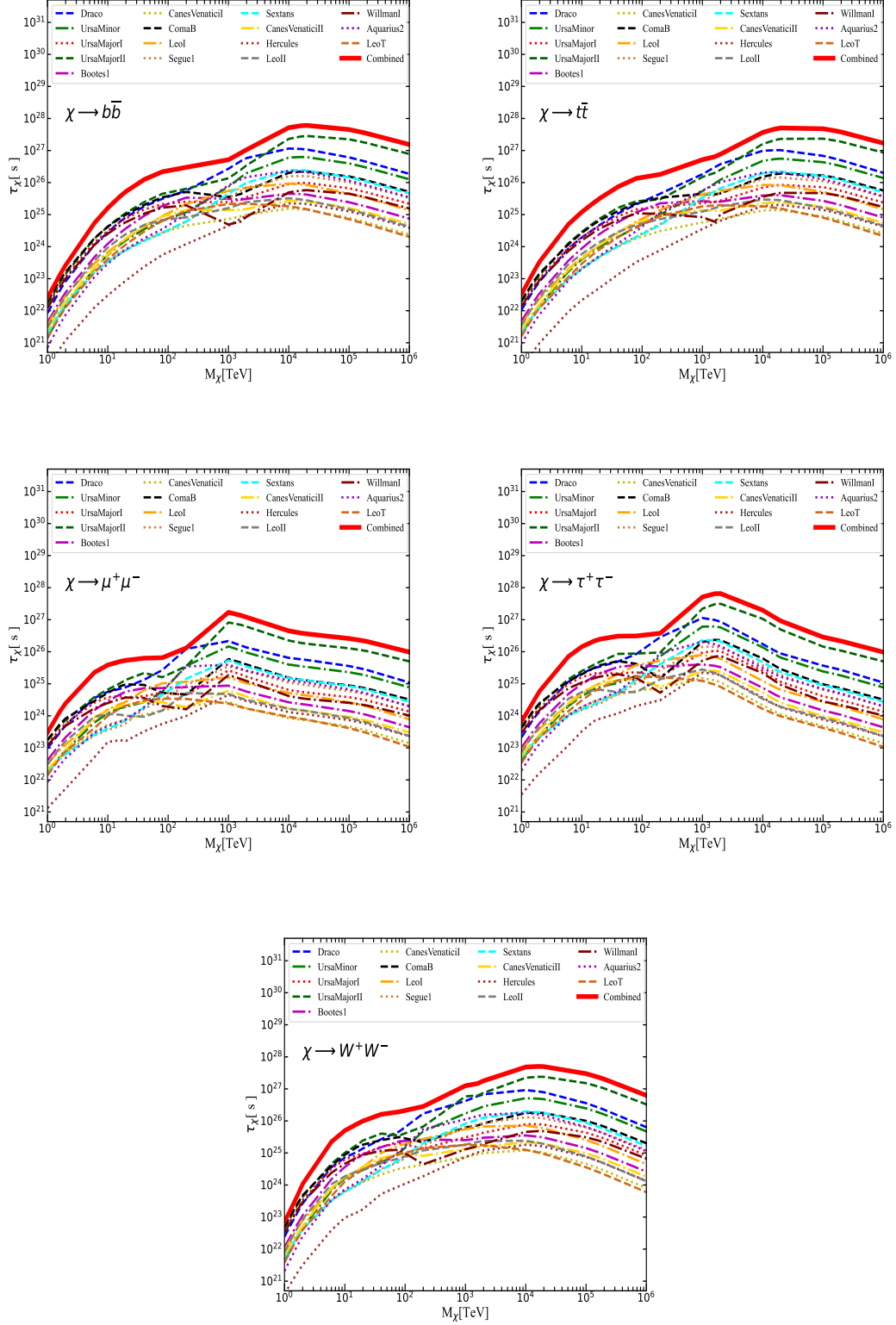


FIG. S9. The panels display the 95% C.L. lower limits on the DM decay lifetime assuming DM with mass range from 1 TeV to 1 EeV with 100% branching ratio decay into specific standard model particles ($b\bar{b}$, $\tau^+\tau^-$, $t\bar{t}$, $\mu^+\mu^-$ and W^+W^-) for all 16 dSphs. The solid red line represents the combined limit obtained from the analysis of all dSphs, while the dashed colored lines correspond to the lower limits obtained from the individual analysis of each dSph.

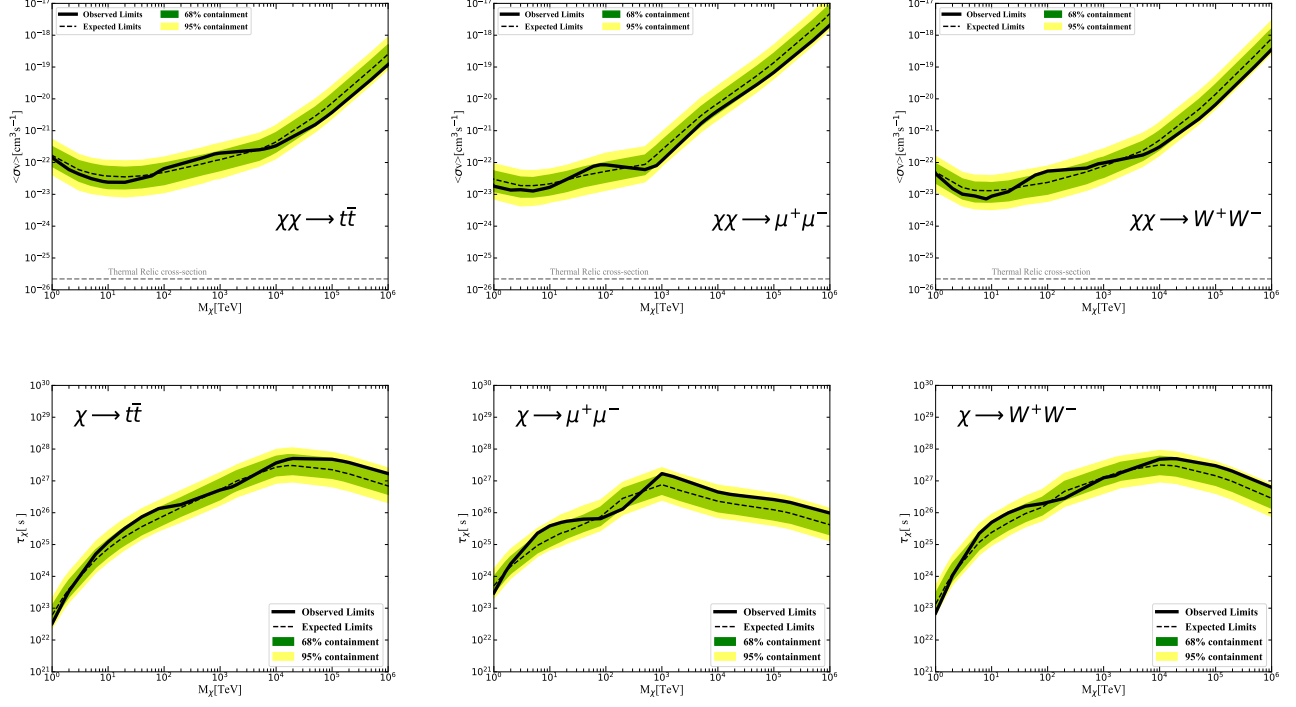


FIG. S10. The comparison of observed limits and expected limits for the $t\bar{t}$, $\mu^+\mu^-$ and W^+W^- processes. The top three figures depict the observed and expected 95% C.L. upper limits on the DM annihilation cross-section. The bottom three figures represent the observed 95% C.L. lower limits on the DM decay lifetime. The solid black line represents the LHAASO observed combined limit, and the dashed black line, green band, and yellow band represent the expected combined limits, their 1σ and 2σ uncertainty based on the mock observations.